Journal of Materials Chemistry B

ROYAL SOCIETY OF CHEMISTRY

PAPER

View Article Online
View Journal

Cite this: DOI: 10.1039/d5tb01168j

Ultra-fast and multi-responsive anisotropic nanofibrous actuator with remote control†

Zijun Zhu,[a] Lantao He,[a] Tingxu Guo,[a] Tong Shao,[a] Jianwu Lan,[a] Shaojian Lin,[a] Patrick Theato *[bc] and Jiaojiao Shang *[ad]

The development of high-performance soft actuators capable of integrating multimodal responsiveness, ultrafast actuation, and programmable deformation remains a critical challenge in soft robotics, primarily due to inherent limitations in current hydrogel-based and elastomer-based systems. These conventional actuators often suffer from compromised functionality, slow response kinetics, and complex fabrication processes. Herein, we present an anisotropic nanofibrous actuator platform that overcomes these limitations through the synergistic combination of structurally aligned electrospun nanofibers and multi-stimulus responsive polymer composites. Our design uniquely integrates three independent actuation mechanisms—thermoresponsive poly(*N*-isopropyl acrylamide-*co*-4-acryloyl benzophenone) (P(NIPAM-*co*-ABP)), photothermally active gold nanoparticles, and pH-sensitive poly(diethylaminoethyl methacrylate-*co*-methyl methacrylate-*co*-4-acryloyl benzophenone) (P(DEAEMA-*co*-MMA-*co*-ABP))—within an oriented nanofibrous architecture. Precise control of fiber alignment through electrospinning techniques enables programmable directional bending responses, while the bilayer configuration facilitates asymmetric deformation through differential swelling behavior. The highly porous nanofibrous network architecture provides rapid mass transport pathways, yielding exceptional actuation speeds (<0.3 s, 360°) that surpass conventional hydrogel-based systems. Furthermore, the actuator still maintains its rapid responsiveness in the air (4 s, 35°). Additionally, the aligned nanofiber morphology contributes to remarkable mechanical robustness, supporting loads up to 178 times its own mass. This work establishes a versatile materials platform that addresses critical challenges in soft robotics by combining multimodal environmental responsiveness, ultrafast actuation kinetics, and programmable deformation control through a scalable fabrication approach. The design principles demonstrated here provide new opportunities for developing advanced soft robotic systems with biomimetic functionality and enhanced performance characteristics.

Received 16th May 2025,
Accepted 23rd June 2025

DOI: 10.1039/d5tb01168j

rsc.li/materials-b

1. Introduction

Soft actuators have emerged as transformative technologies in biomedical[1] and robotic[2] applications, integrating the adaptability of biological systems with engineered functionality. Inspired by natural actuation mechanisms, stimuli-responsive polymers capable of undergoing reversible physicochemical changes in response to thermal,[3] pH,[4,5] ionic,[6] light,[7–9] or acoustic stimuli[10] have become fundamental building blocks for intelligent soft actuators. While these polymers have enabled significant advancements, existing soft actuator systems face inherent challenges in simultaneously achieving rapid response, multi-stimuli sensitivity, and programmable deformation,[11] which severely restricts the application of soft actuators. For practical applications such as drug delivery systems, multi-stimuli responsiveness is indispensable to decouple targeting and release processes. Conventional hydrogel-[12] or film-based[13,14] actuators typically suffer from slow response times due to diffusion-limited mass transport, while achieving rapid responses often requires additional pore-forming treatments of hydrogels or the use of porous templates during fabrication, which introduces process complexity and potential toxicity from hazardous reagents. For examples, Wang *et al.* used 4D printing technology to biologically replicate anisotropic NIPAM-based hydrogel. The hydrogel deforms in water over several minutes.[15] Chen *et al.* fabricated a swimming hydrogel actuator using carbon dots with rotatable symmetrical

[a] College of Biomass Science and Engineering, Sichuan University, Chengdu, Sichuan 610065, China. E-mail: jiaoj.shang@scu.edu.cn
[b] Soft Matter Synthesis Laboratory, Institute for Biological Interfaces 3 (IBG-3), Karlsruhe Institute of Technology (KIT), Eggenstein-Leopoldshafen 76344, Germany. E-mail: patrick.theato@kit.edu
[c] Institute for Chemical Technology and Polymer Chemistry (ITCP), Karlsruhe Institute of Technology (KIT), Karlsruhe 76131, Germany
[d] National Engineering Laboratory for Clean Technology of Leather Manufacture, Sichuan University, Chengdu, Sichuan 610065, China

† Electronic supplementary information (ESI) available. See DOI: https://doi.org/10.1039/d5tb01168j

surfaces. The petal-shaped actuator could flip underwater in 30 minutes.[16] Additionally, complex anisotropic structures often require intricate fabrication processes, limiting their scalability and practicality.

Nature offers elegant solutions to these challenges through sophisticated material architectures. For instance, the humidity-driven twisting of wheat awns, facilitated by oriented cellulose fibrils,[17] and the rapid leaf-folding mechanism of *Mimosa pudica*, governed by specialized motor cells,[18] demonstrate how anisotropic structures enable complex, directional movements through simple hydration changes. Inspired by these natural mechanisms, researchers have developed a variety of biomimetic structures, including bilayers,[19] gradient structures,[20] patterned structures,[21] and oriented structures,[22] among others.[23–28] Many of these designs leverage water absorption and dehydration as a driving force, mimicking plant motion. For example, wheat awns contain tissues with differently oriented cellulose fibrils, where localized non-uniform swelling and shrinking drive rotational movement. This simple yet effective directional actuation has inspired numerous biomimetic designs. Similarly, He *et al.* developed a directional deformation hydrogel actuator inspired by *Mimosa pudica*, which contracts along the alignment direction of its cells in response to external stimuli.[29] However, despite their potential, the fabrication of anisotropic structures often remains complex and requires stringent processing conditions.[30]

To address these challenges, we herein present a novel composite nanofibrous bilayer actuator fabricated through a facile and scalable electrospinning approach. This actuator exhibits multiple responsiveness, ultrafast actuation, anisotropic deformation, and remarkable load-bearing capacity. Programmable 3D deformation is achieved through asymmetric expansion between distinct layers and the controlled orientation in the horizontal direction of responsive polymer fibers (Fig. 1a). This versatile yet facile fabrication strategy for nanofibrous bilayer actuators represents a significant step forward in the development of high-performance actuators with multi-responsiveness, controllable deformation, remote actuation, and enhanced mechanical properties (Fig. 1b).

2. Experimental section

2.1. Materials

N-Isopropyl acrylamide (NIPAM, 97%) was purchased from Sigma-Aldrich and recrystallized from a solvent mixture of toluene and *n*-hexane (3 : 2 volume ratio). Glycidyl methacrylate (GMA, 98%) was purified using a neutral aluminum oxide column. Diethylaminoethyl methacrylate (DEAEMA, 98.5%) and methyl methacrylate (MMA, 99%) were obtained from Sigma-Aldrich. 2,2′-Azobisisobutyronitrile (AIBN) was recrystallized twice from methanol. Gold(III) chloride trihydrate ($HAuCl_4 \cdot 3H_2O$, 99%) was sourced from Titan Technology Co., Ltd. Toluene and methanol were purchased from Sigma-Aldrich. Epigallocatechin gallate (EGCG) was obtained from Nanjing Duolon Biotechnology Co., Ltd. Ultrapure water (18.2 MΩ cm, Millipore) was used for all experiments. 4-Acryloyl benzophenone (ABP), 2,6-lutidine, acryloyl chloride, rhodamine B, and other reagents were purchased from Sigma-Aldrich and used without further purification.

2.2. Characterization

UV-Vis absorption spectra were recorded using a Jasco V-630 spectrophotometer over a wavelength range of 200–900 nm. Transmission electron microscopy (TEM) images were obtained using a JEOL JEM-1011 transmission electron microscope. Scanning electron microscopy (SEM) images were acquired using a Zeiss EVO-MA 10 microscope operating at 5 kV. Prior to SEM imaging, all samples were freeze-dried using an Alpha

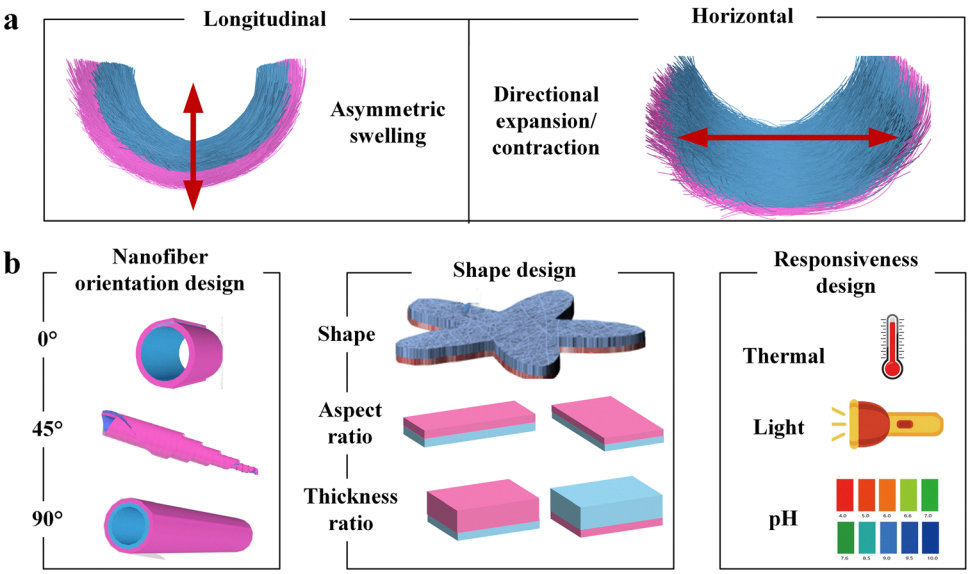

Fig. 1 (a) Schematic diagram of the deformation mechanism of the actuator; (b) the approach to modulating the responsiveness of actuators through modular design.

2-4 LD Plus freeze dryer and sputtered with carbon. Micro-differential scanning calorimetry (Micro-DSC) was performed using a MicroCal VP-DSC in the temperature range of 0–50 °C. Fourier-transform infrared spectroscopy (FT-IR) was used to analyze the functional groups (Thermo Scientific Nicolet iS10), and proton nuclear magnetic resonance (^{1}H NMR) spectroscopy was employed to determine the structural composition of the synthesized polymers (Bruker AV, the solvent is DMSO-d_6). An 808 nm near-infrared (NIR) light source (VLSM-808-B-8-FA, Shanghai Hanyu Optical Fiber Communication Technology Co., Ltd) was used for photothermal actuation experiments. Thermogravimetric analysis (TGA) was conducted using a Netzsch TG 209 Fi Libra thermogravimetric analyzer (Netzsch Scientific Instruments Trading Co., Ltd, Shanghai, China) under a nitrogen atmosphere, with a heating rate of 10 °C min^{-1} from 20 °C to 600 °C.

2.3. Synthesis of gold nanoparticles

Gold nanoparticles (AuNPs) were synthesized using EGCG as a natural reducing and stabilizing agent. A 0.84 mL aliquot of 0.5 mM $HAuCl_4{\cdot}3H_2O$, aqueous solution was added to a vial and stirred at 2000 rpm. Subsequently, 0.16 mL of 0.8 mg mL^{-1} EGCG aqueous solution was added, and the mixture was stirred at room temperature for 30 min.

2.4. Synthesis of polymers for electrospinning

4-Acryloyl benzophenone (ABP) was used as a photo-crosslinker. Poly(glycidyl methacrylate-*co*-4-acryloylbenzophenone) P(GMA-*co*-ABP) was synthesized according to a previously reported procedure.[18] The synthesis of P(NIPAM-*co*-ABP) was carried out as follows: NIPAM (2 g, 17.674 mmol), ABP (0.138 g, 0.547 mmol), and AIBN (0.0299 g, 0.182 mmol) were dissolved in 5 mL of 1,4-dioxane in a 10 mL reaction vial equipped with a magnetic stirrer. The solution was purged with nitrogen for 30 min and then heated in an oil bath at 70 °C overnight. The reaction mixture was subsequently cooled to room temperature, diluted with tetrahydrofuran (THF), and precipitated in an excess of hexane to isolate the copolymer. This purification process was repeated three times. The final polymer was dried in a vacuum oven at 40 °C for 48 h, yielding 93%. Similarly, the synthesis of P(DEAEMA-*co*-MMA-*co*-ABP) was conducted by sequentially adding pre-measured amounts of DEAEMA and MMA (after stabilizer removal) into a round-bottom flask along with ABP, AIBN, and dioxane. The mixture was purged with nitrogen for 30 min and then heated in a 70 °C oil bath overnight.

2.5. Preparation of the bilayer fibrous membrane

As illustrated in Fig. 2, the passive bottom layer was first prepared by electrospinning a well-mixed solution of

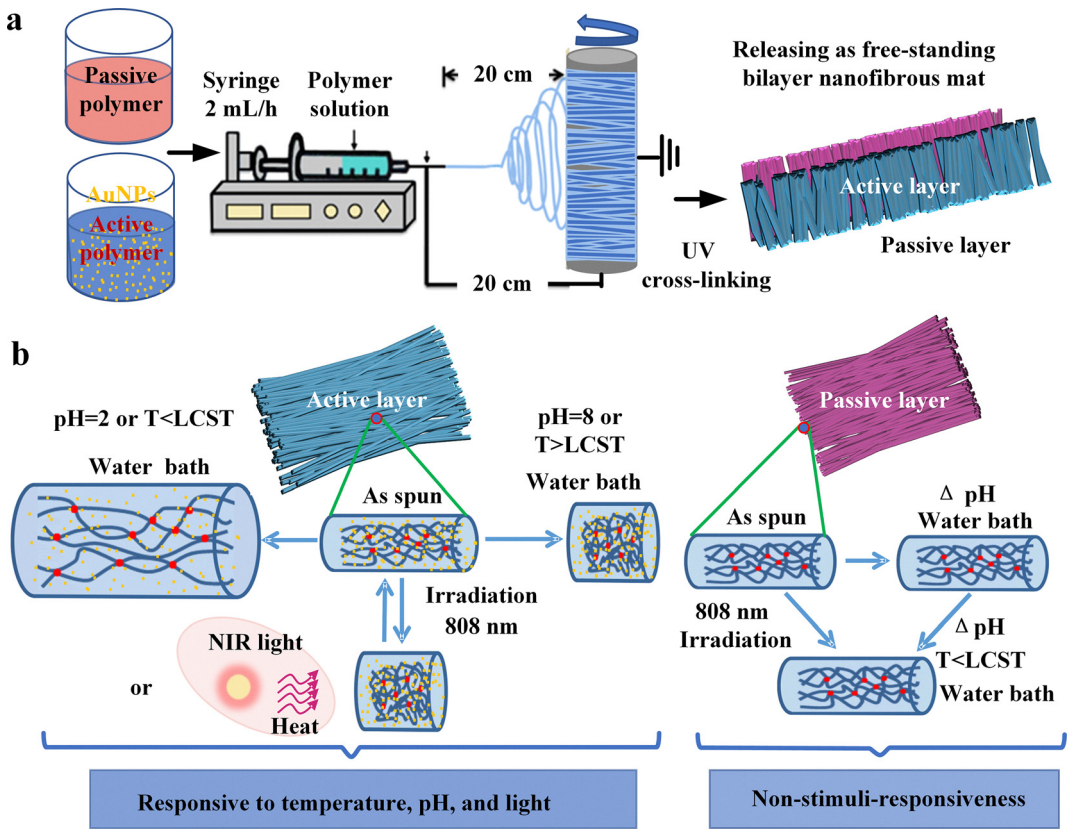

Fig. 2 (a) Schematic illustration of the fabrication of oriented bilayer nanofibrous actuators using electrospinning polymers; (b) detailed illustration of responsive behaviors of separated layers upon heating, adjusting pH, and irradiation of NIR at 808 nm wavelength.

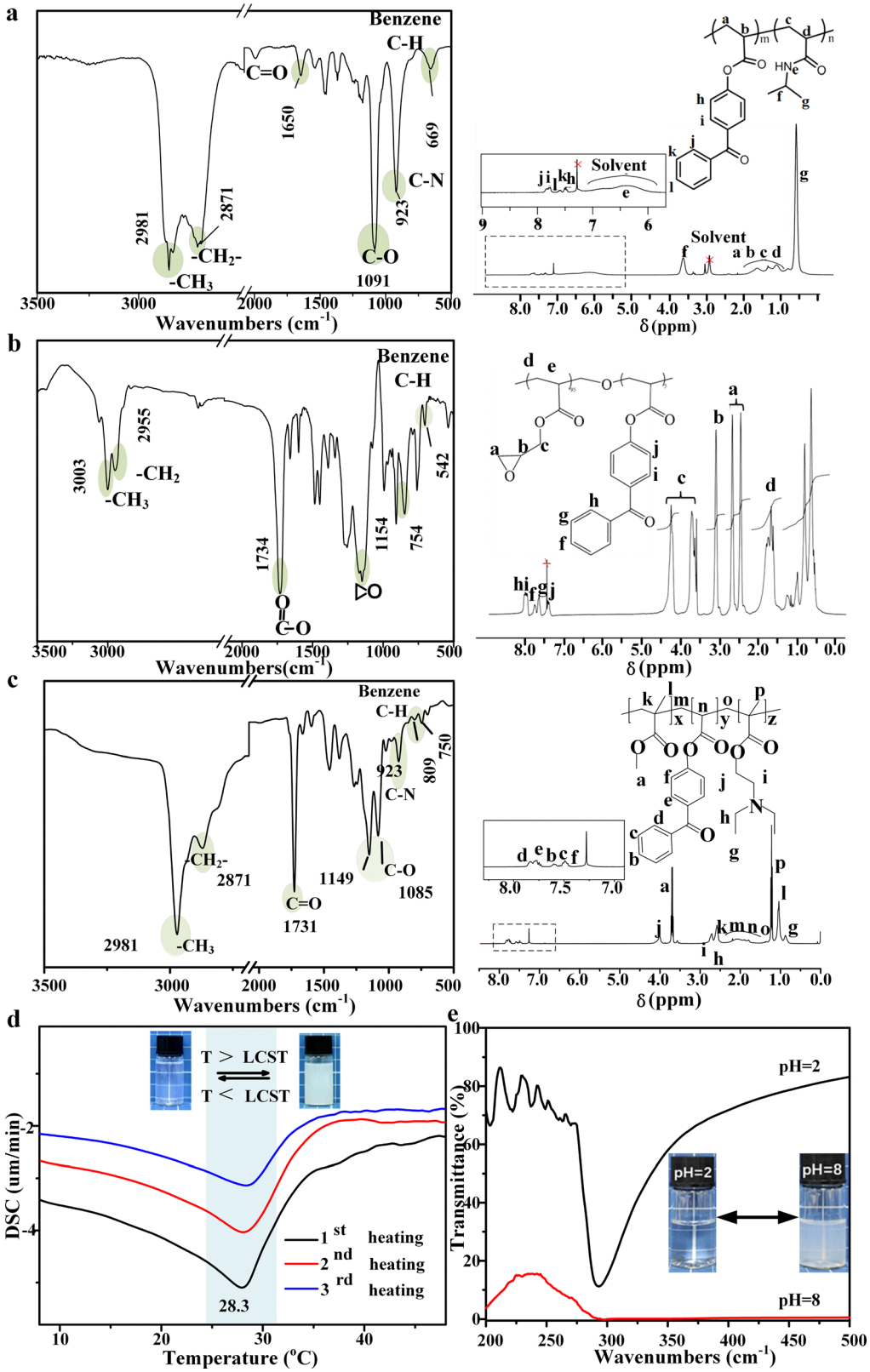

Fig. 3 (a) FT-IR and ^{1}H-NMR spectra of P(NIPAM-*co*-ABP); (b) FT-IR and ^{1}H-NMR spectra of P(GMA-*co*-ABP); (c) FT-IR and ^{1}H-NMR spectra of P(DEAEMA-*co*-MMA-*co*-ABP); (d) micro-DSC measurement of cross-linked P(NIPAM-*co*-ABP) fibrous membrane showing LCST around 28.3 °C; (e) transmittance of P(DEAEMA-*co*-MMA-*co*-ABP) solutions under different pH.

P(GMA-*co*-ABP) (35 wt%) and 0.3 wt% rhodamine B in a DMF/THF (3 : 7 by volume) solvent mixture. On top of the electrospun P(GMA-*co*-ABP) nanofibers, a uniformly mixed solution of 30 wt% P(NIPAM-*co*-ABP) and AuNPs in DMF/THF (1 : 1 by volume) was electrospun as the active layer. Electrospinning was conducted using a 0.8 mm diameter needle at an applied voltage of 22 kV, with a syringe pump flow rate of 1.5 mL h^{-1}. The needle tip-to-collector distance was set at 25 cm.

The electrospun nanofibrous membrane was dried overnight at room temperature under external pressure. Crosslinking was then initiated by continuous UV illumination (λ = 300–400 nm, 40 W) for 2 h. The crosslinked nanofibrous membranes were used in subsequent experiments to evaluate actuation behavior by alternating immersion in water at 4 °C and 40 °C or by exposure to 808 nm NIR light. SEM was employed to analyze the resulting nanofiber morphologies. The pH-responsive layer was fabricated following the same procedure as the PGMA layer, replacing P(GMA-*co*-ABP) with P(DEAEMA-*co*-MMA-*co*-ABP).

2.6. Actuation characterization

Thermally induced actuation of the nanofibrous membranes was evaluated by alternately immersing the samples in water at 4 °C and 40 °C. pH-Responsive actuation was investigated by sequentially immersing the nanofiber membranes in aqueous solutions at pH 2 and pH 8. For light-driven actuation, the nanofibrous membranes were exposed to an 808 nm laser at different angles, and their bending behavior was recorded using a camera. The changes in bending angle were analyzed to assess actuation performance.

3. Results and discussions

To achieve such a polymer fiber responsive array, poly(*N*-iso propyl acrylamide-*co*-4-acryloyl benzophenone) (P(NIPAM-*co*-ABP)) embedded with gold nanoparticles (AuNPs) and poly(glycidyl methacrylate-*co*-ABP) (P(GMA-*co*-ABP)) were separately electrospun to generate oriented nanofibrous membranes (Fig. 2a). These two layers were then overlaid, subjected to controlled pressure, and ultraviolet-crosslinked to form a bilayer-structured directional actuator, with PNIPAM serving as the active layer and PGMA as the passive layer (Fig. 2b). Building upon this platform, a layer-substitution strategy was implemented by electrospinning pH-responsive poly(diethylaminoethyl methacrylate) (PDEAEMA) to replace PGMA, resulting in a triply responsive actuator that integrates thermo-responsivity (PNIPAM), AuNP-based photothermal responsiveness, and pH sensitivity. This electrospun nanofibrous membrane actuator enables anisotropic actuation through computer-aided fiber orientation and actuator shape design. Additionally, the high porosity of electrospun nanofiber membranes enhances mass and heat transfer efficiency, leading to ultrafast deformation. Furthermore, the actuator exhibits excellent load-bearing capacity due to the reinforcement provided by the oriented fibers.

3.1. Characterization of stimuli-responsive polymers

Three random copolymers, thermoresponsive P(NIPAM-*co*-ABP), non-responsive P(GMA-*co*-ABP), and pH-responsive P(DEAEMA-*co*-MMA-*co*-ABP), were synthesized (Fig. 3a–c). The pH-responsive DEAEMA exhibited limited thermal stability and processability due to its low glass transition temperature (T_g). To enhance rigidity, we incorporated methyl methacrylate (MMA), which features a sterically hindered quaternary carbon backbone, and ABP, to enable photo cross-linking, both significantly improving the thermal stability of P(DEAEMA-*co*-MMA-*co*-ABP) (> 300 °C, Fig. S1, ESI†). Micro-DSC analysis of aqueous P(NIPAM-*co*-ABP) revealed a broad endothermic transition initiating at 20 °C and peaking at 28.3 °C (Fig. 3d), indicative of its lower critical solution temperature (LCST). As Fig. S2 (ESI†) shows, the observed LCST of P(NIPAM-*co*-3% ABP) at 28 °C was lower than that of pure PNIPAM due to hydrophobic ABP interactions, which disrupt the polymer-water hydrogen bonding network, accelerating the coil-to-globule transition. The observed LCST elevation in P(NIPAM-*co*-ABP) upon AuNPs incorporation is attributed to enhanced hydrophilicity from hydrogen bonding between phenolic hydroxyl groups on AuNP surfaces and PNIPAM chains, which stabilizes the hydration layer, requiring elevated temperature for phase transition. Adjusting the ABP molar ratio and the content of AuNPs fine tunes the temperature response range.

The pH-responsiveness of P(DEAEMA-*co*-MMA-*co*-ABP) is governed by the protonation–deprotonation equilibrium of its tertiary amine groups. Under acidic conditions, protonation enhances hydrophilicity, resulting in a transparent solution, whereas deprotonation at alkaline pH induces hydrophobic aggregation, leading to macroscopic turbidity (Fig. 3e). This reversible solubility transition facilitates programmable actuation through pH-triggered hydration state modulation.

3.2. Characterization of stimuli-responsive nanofiber membranes

We fabricated multi-responsive actuators using electrostatically aligned nanofiber membranes. A bilayer structure was created *via* electrospinning: the active layer consisted of P(NIPAM-*co*-ABP) mixed with AuNPs, while the passive layer comprised P(GMA-*co*-ABP). The PGMA passive layer was selected for its excellent mechanical properties, temperature-inert behavior, and chemically reactive epoxy groups, enabling post-synthetic functionalization.

Monodispersed AuNPs and their aggregates within the nanofibers were characterized *via* TEM image (Fig. 4a). The average diameter of synthesized monodispersed AuNPs dispersed in water was approximately 10–20 nm, as measured by Nano Measure. Then, the optical characterization of AuNPs before and after mixing with P(NIPAM-*co*-ABP) was conducted. Optical absorption peaks around 580 nm were observed for both monodispersed AuNPs and P(NIPAM-*co*-ABP)–AuNPs (Fig. 4b). Increasing P(NIPAM-*co*-ABP) concentrations resulted in a red shift and peak broadening, indicating AuNP aggregation (Fig. 4c). After demonstrating the responsiveness of the

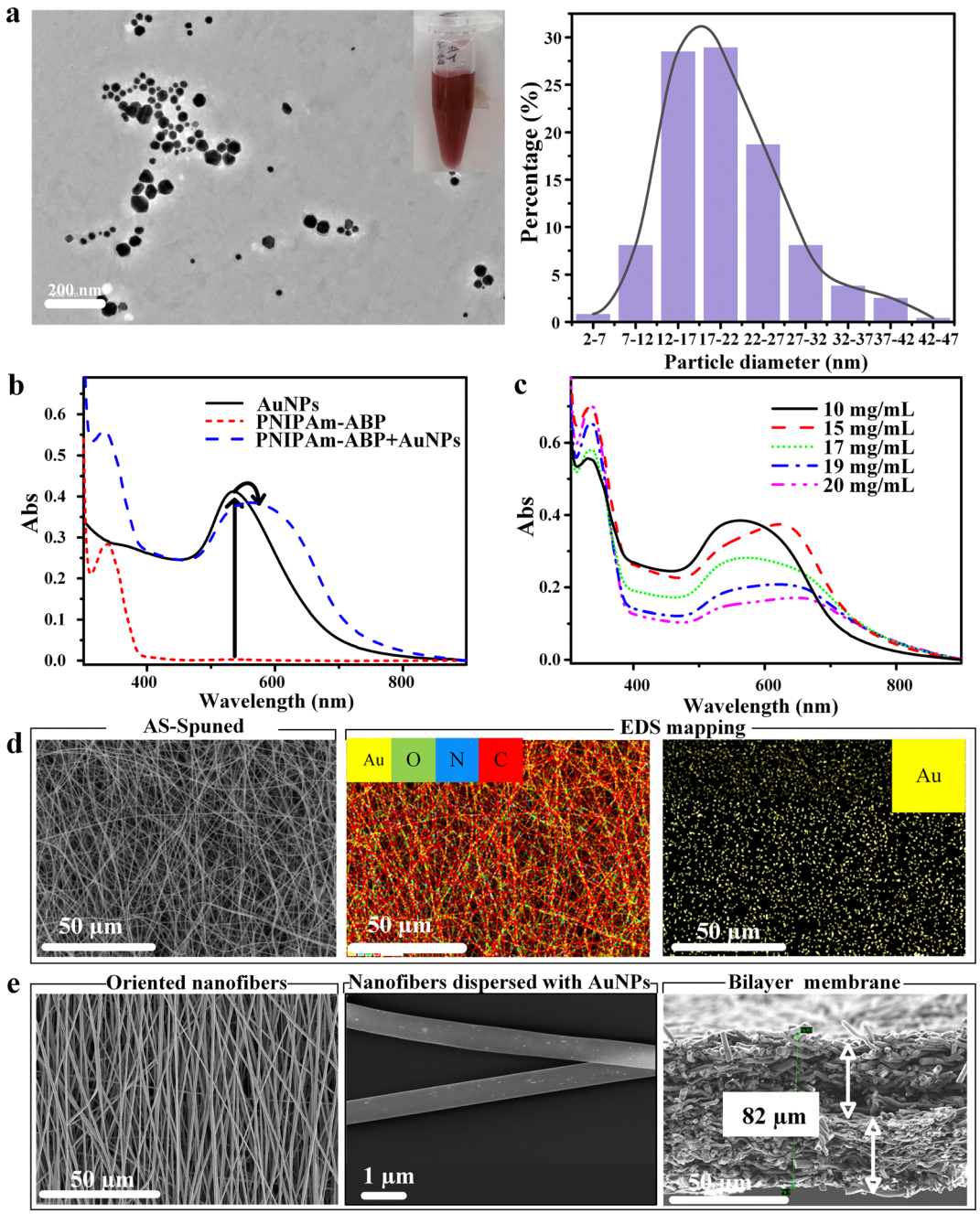

Fig. 4 (a) TEM image of AuNPs synthesized by EGCG and distribution analyzed by nano measure; (b) UV-Vis spectra of AuNPs, P(NIPAM-*co*-ABP) and P(NIPAM-*co*-ABP) mixed AuNPs in toluene; (c) UV-Vis spectra of P(NIPAM-*co*-ABP) mixed AuNPs with increasing the mixed concentration of P(NIPAM-*co*-ABP); (d) SEM images of nanofiber morphologies and EDX elemental mapping for AuNPs in the nanofibers; (e) SEM of oriented nanofibers and the cross-sectional view of the bilayer membrane.

synthesized copolymers, electrospinning followed by pressing enhanced membrane stability and prevented delamination after photo-crosslinking. The resultant bilayer system, consisting of PGMA and PNIPAM nanofibers embedded with AuNPs and oriented at different angles, was designed for directional movement control. As illustrated in Fig. 4d, the electrospun nanofibers exhibited a uniform diameter without bead formation. Additionally, energy dispersive X-ray spectroscopy (EDX) mapping of the nanofibers provided elemental signals for gold was measured, indicating uniform dispersion of AuNPs within the nanofibers. As shown in Fig. 4e, the morphology of the nanofibers showed a high degree of orientation, as anticipated. High-resolution SEM visualized the surface morphology of P(NIPAM-*co*-ABP) nanofibers embedded with AuNPs (Fig. 4e and Fig. S3, inset, ESI†). Additionally, the cross-sectional view of SEM supported the bilayer membrane structure of the actuator.

3.3. Multiple responsiveness actuator design with controllable deformation

To investigate the multi-response and programmable actuation characteristics of aligned nanofibrous actuators, we systematically examined the deformation behavior of nanofibrous actuators under thermal (4 °C and 40 °C), light (808 nm), and pH (pH 2 and pH 8) stimuli. Additionally, we explored the impact of structural parameters, such as the shape and thickness ratios of different layers, on actuation performance to gain a deeper understanding of their driving mechanisms. First, P(NIPAM-*co*-ABP) fibers exhibited swelling when cooled to 4 °C and shrinking when heated to 40 °C (Fig. S4a–c, ESI†), whereas P(GMA-*co*-ABP) fibers showed no significant response to changes in temperature (Fig. S4d–f, ESI†). This contrast confirmed that the deformation of the actuator originates from the differential expansion and contraction between the active and passive layers. To further analyze directional actuation, we fabricated nanofiber membrane actuators with fiber alignments at 0°, 45°, and 90° relative to the long axis (Fig. 5a). Notably, when the P(NIPAM-*co*-ABP) layer was aligned at 0°, the actuator stretched along the fiber direction at 4 °C (below LCST), causing it to bend sideways. Conversely, immersion in 40 °C water (above LCST) led to a change in the actuation mode, with the hook-shaped structure unfolding and subsequently curling perpendicularly due to the contraction of the P(NIPAM-*co*-ABP) layer (Fig. 5b). This deformation was fully reversible over 50 thermal cycles, demonstrating excellent structural integrity without delamination (Movie S1, ESI†). Similarly, distinct deformation patterns were observed in actuators with fiber orientations at 45° and 90°, highlighting the crucial role of fiber alignment for programmable actuation.

To assess the light responsiveness of these actuators, we integrated AuNPs into the thermoresponsive layer and compared their actuation behavior under 808 nm laser irradiation with and without AuNPs (Movie S2, ESI†). The absence of deformation in actuators lacking AuNPs confirmed that the photoresponse arose from the photothermal conversion effect of AuNPs. To further investigate programmable photothermal actuation, we placed actuators with different fiber orientations under focused light exposure. As shown in Fig. 5c, localized heating generated by AuNPs induced asymmetric expansion of the active layer, leading to diverse curling directions as the temperature exceeded the LCST of PNIPAM nanofibers.

To extend the functionality of the actuator beyond dual-stimuli responses, we replaced the P(GMA-*co*-ABP) layer with a pH-responsive P(DEAEMA-*co*-MMA-*co*-ABP) nanofiber membrane. This substitution maintained the mechanical stability of the bilayer while introducing pH sensitivity, enabling a triple-stimuli-responsive system. The successful integration of pH responsiveness was validated by controlled actuation behavior at pH 2 and pH 8 (Fig. S5, ESI†). Furthermore, to determine the impact of shape on actuation dynamics, we fabricated rectangular actuators with varying aspect ratios (5 : 1 to 5 : 4) and submerged them in an HCl solution (pH = 2). As illustrated in Fig. 6a, the response time increased from 31.9 s for the 5 : 1 aspect ratio to 50.6 s for the 5 : 4 configuration, indicating that

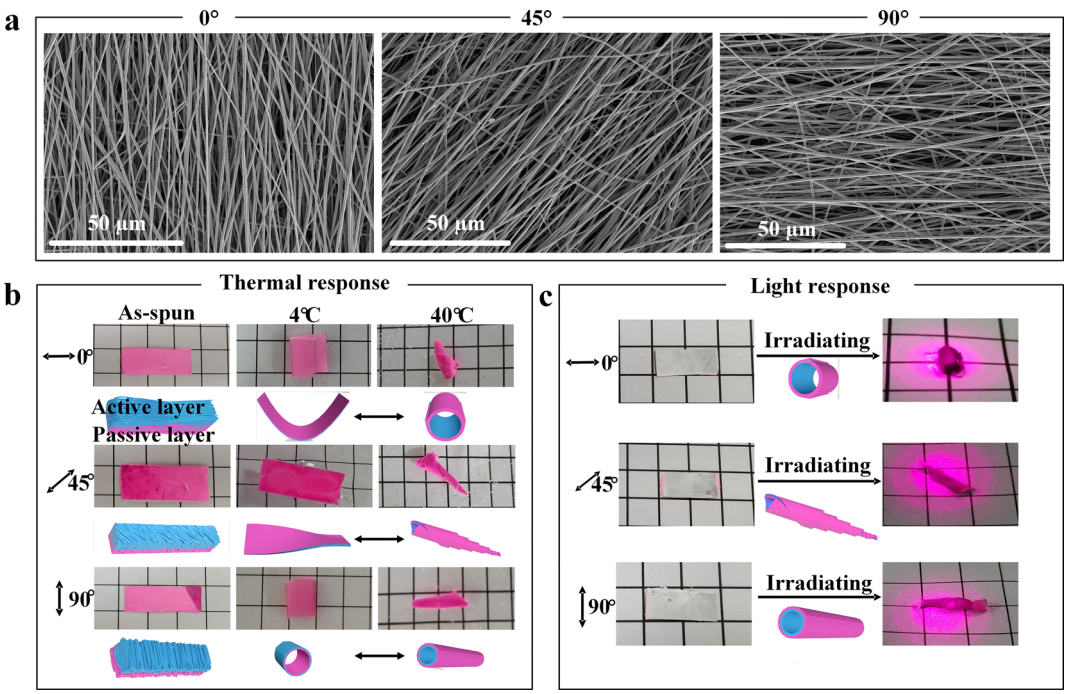

Fig. 5 (a) SEM images of nanofiber membranes arranged along different angles; (b) temperature-driven behaviors of bilayers composed of P(NIPAM-*co*-ABP)/AuNP (blue) and P(GMA-*co*-ABP) (pink) with varying fiber orientations: 0°, 45°, and 90° relative to the long axis of the membrane; (c) photoresponse behaviors of bilayer systems with fiber orientations: 0°, 45°, and 90° relative to the long axis. P(NIPAM-*co*-ABP)/AuNP (blue) and P(GMA-*co*-ABP) (pink). Scale bar: 5 mm.

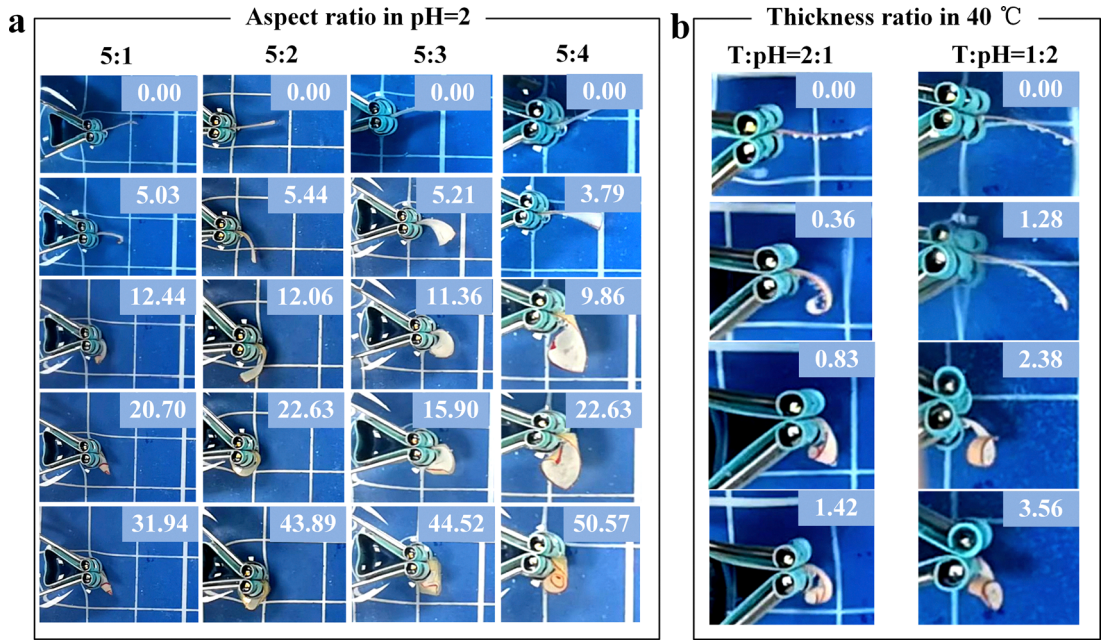

Fig. 6 (a) Driving behavior and time for bilayer (yellow for pH layer and white for temperature layer) fibrous membranes with different aspect ratios; (b) driving behavior and time for bilayer (yellow for pH layer and white for temperature layer) fibrous membranes with varying ratios of thickness. Scale bar 1.0 cm.

higher aspect ratios promote faster actuation due to increased anisotropic stress differences and reduced resistance as the volume decreases. In addition, to further explore the potential for programmable deformation, we designed a petal-shaped actuator using computer-aided laser cutting (Fig. S6, ESI†). This shape customization enabled more complex deformation patterns beyond simple bending, as demonstrated by a flower-shaped actuator capable of reversible folding and expansion under external stimuli (Movie S3, ESI†). Additionally, we investigated how the thickness ratio between active and passive layers influenced actuation kinetics. As shown in Fig. 6b and Fig. S7 (ESI†), an optimal 2 : 1 active-to-passive layer thickness ratio resulted in the fastest actuation, as the dominant active layer generated stronger intrinsic stress gradients, enhancing overall responsiveness.

3.4. Characterization of the rapid response of the actuators

Response speed is a critical parameter for actuators, directly influencing their practical applications in dynamic environments. As demonstrated in Fig. 7a and Fig. S8, Movie S4 (ESI†), the actuation kinetics of the nanofiber membrane actuators significantly outperformed conventional hydrogel-based systems, achieving sub-second response time with a rapid deformation of 0.3 s (360°) in 40 °C water (Table 1). To further assess their responsiveness under non-aqueous conditions, we conducted a laser-induced curvature analysis in air. The results, shown in Fig. 7b, indicate that the actuator completed deformation within seconds, and Movie S5 (ESI†) confirmed that this photo-responsive actuation was fully reversible, demonstrating excellent repeatability and stability over multiple cycles. Remarkably, when subjected to NIR irradiation (808 nm, 0.15 W cm^{-2}), the actuator exhibited exceptional photothermal actuation performance. It was capable of lifting 178 times its own mass, while achieving a contraction of 44% rapidly within seconds (Fig. 7c). This remarkable actuation capacity is attributed to the highly oriented nanofiber architecture, which significantly enhances mechanical performance by promoting efficient stress transfer and maintaining structural integrity under load. The ability to manipulate objects across a wide range of mass scales underscores the suitability of actuators for operation in demanding environments. Even in extreme micro-environments, the actuator demonstrated the ability to load, transport, and propel relatively heavy objects despite its small size and lightweight nature.

To evaluate whether the actuator retained its ultrafast response speed after structural modifications, we replaced the PGMA passive layer with a pH-responsive layer. As shown in Fig. 7d and Fig. S9 (ESI†), the actuator maintained its rapid deformation kinetics, with response times remaining within the sub-second to second range across all stimuli. This result confirmed that the electrospinning-enabled fabrication strategy not only enabled the construction of multi-stimuli-responsive actuators but also preserved their rapid dynamic performance. As anticipated, the high porosity of the electrospun nanofibrous bilayer played a crucial role in facilitating ultra-fast actuation, significantly surpassing the response speed of tens of seconds or more of conventional hydrogel-based actuators.[31,32,34] This design strategy establishes a universal platform for the development of multifunctional soft actuators, where programmable responsiveness can be precisely tailored through rational material selection and optimized layer configurations. The demonstrated synergy between

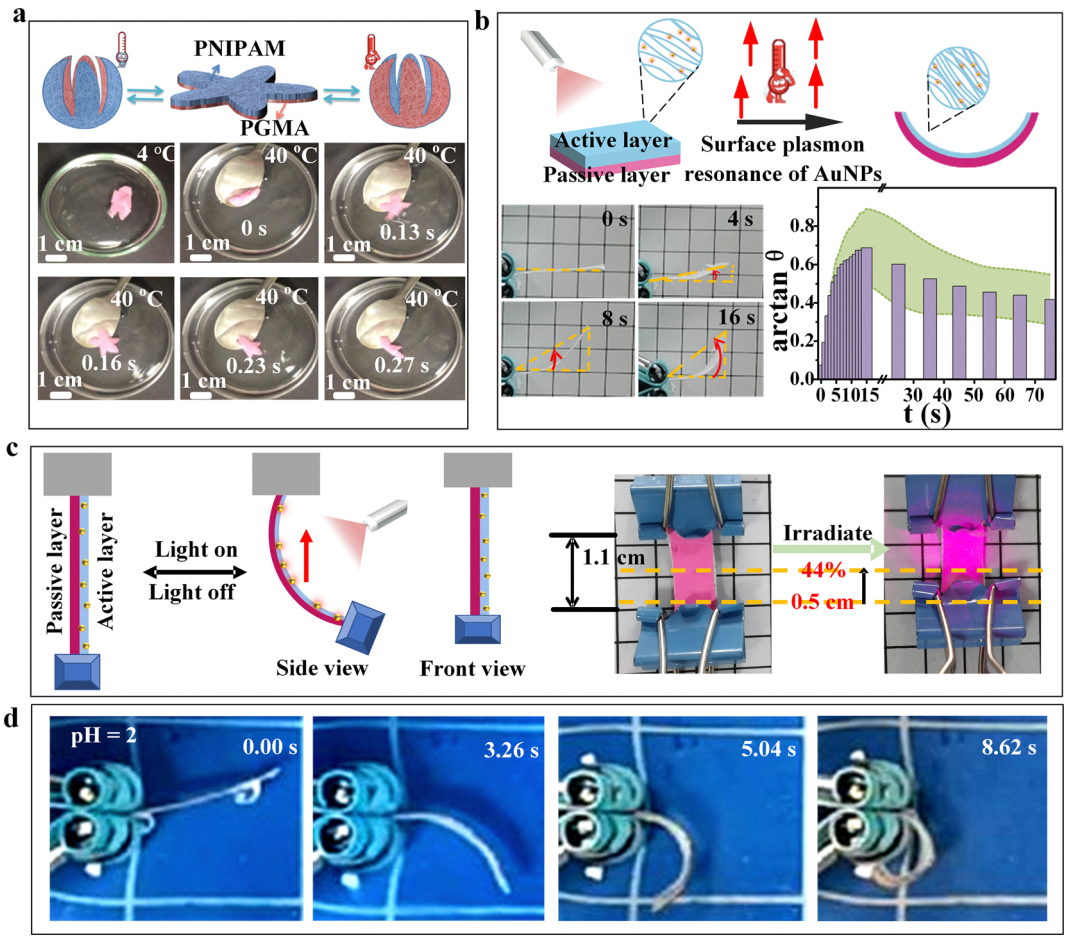

Fig. 7 (a) Schematic of reversible petal-shaped actuator flipping with temperature changes and photographs showing ultrafast deformation of the nanofibrous bilayer membrane in water at 4 °C and 40 °C; (b) the scheme and photographs of nanofiber membranes responding to light, and the curvature-time plot of the bilayer nanofiber membrane under laser irradiation; (c) the scheme and photographs of the bilayer nanofibrous membrane lifting a clamp (1229 mg, 178 times its own weight) upon 808 nm laser irradiation (0.15 W cm^{-2}); (d) photographs of the deformation of bilayer fibrous membranes in pH = 2, featuring a pH-responsive layer (yellow) and a temperature-responsive layer (white). Scale bar: 0.5 cm.

Table 1 Typical performance parameters of the soft actuators

Sample	Response time	Multi-responsiveness	Complexity of preparation	Year	Ref.
Lignin-polyamide elastomer	2 s	2 (Light-temp.)	M	2022	28
Electrospun LCEs	3 s	2 (Light-temp.)	M	2024	31
$Ti_3C_2T_x$/PNIPAM hydrogels	10 s	2 (Light-temp.)	M	2023	29
Polyelectrolyte hydrogels	min	1 (Elec.)	M	2022	32
Electrospun PNIPAM/PAN/Fe_3O_4	178° s^{-1}	3 (Light-temp.-mag.)	L	2021	33
CNT-PE	1–10 s	4 (Light-temp.-Elec.-H)	H	2022	7
PAN hydrogels	30 s	1 (pH)	L	2023	4
LCEs hydrogels	min	2 (Light-temp.)	H	2022	34
4D-printed hydrogels	min	2 (Light-temp.)	H	2021	15
Electrospun all-fiber	0.67 cm s^{-1}	3 (Light-temp.-H.)	L	2025	35
This work	**0.3 s/360°**	**3 (Light-temp.-pH)**	**L**	—	—

PNIPAM: poly(*N*-isopropyl acrylamide); CNT: carbon nanotubes; PE: polyethylene; PAN: poly(acrylic acid-*co*-*N*-vinylcaprolactam); LCE: liquid crystalline elastomer; H: high; M: middle; L: low; Temp.: temperature; Elec.: electricity; H: humidity; Mag.: magnetism.

rapid response, high mechanical performance, and multi-stimuli adaptability highlights the potential of these actuators for advanced soft robotics, biomedical applications, and smart material systems.

4. Conclusion

In this study, we have successfully developed a multi-responsive actuator with ultrafast response speed, high mechanical stress

tolerance, controlled deformation, and remote light-driven actuation using a simple and universal fabrication strategy. The electrospun nanofiber bilayer actuator, composed of P(NIPAM-*co*-ABP)/AuNPs as the active layer and P(GMA-*co*-ABP) as the passive layer, exhibited high porosity, which enabled rapid and reversible actuation (<0.3 s for complete petal flipping). The incorporation of plant polyphenol-reduced AuNPs into the P(NIPAM-*co*-ABP) matrix imparted photothermal responsiveness, allowing the actuator to maintain fast and reversible deformation even in air, with a bending transition from 0° to 90° occurring within 17 seconds. Furthermore, by replacing the P(GMA-*co*-ABP) passive layer with a pH-responsive P(DEAEMA-*co*-MMA-*co*-ABP) component, we successfully fabricated a triple-stimuli-responsive actuator capable of precise and programmable deformation under thermal, light, and pH variations. The highly oriented nanofiber architecture significantly enhanced mechanical performance, enabling the actuator to lift objects weighing up to 178 times its own mass while preserving structural integrity and actuation efficiency. Unlike conventional hydrogel-based actuators that necessitate intricate design optimizations and precise material tuning for specific applications, this electrospun nanofibrous actuator allowed for an easy customization by integrating new responsive materials. Overall, this modular design strategy provides a scalable and versatile platform for the next generation of programmable soft actuators, paving the way for their application in advanced biomedical devices, soft robotics, and multi-stimuli-responsive systems. By leveraging electrospinning technology and multi-functional nanomaterials, this work establishes a foundation for future innovations in smart actuators with tunable and rapid responsiveness.

Author contributions

Zijun Zhu: conceptualization, investigation, writing – original draft, data curation, project administration, formal analysis, validation methodology, software. Lantao He: formal analysis, validation methodology. Tingxu Guo, Tong Shao: methodology, software. Jianwu Lan, Shaojian Lin: supervision. Patrick Theato: supervision, resources, funding acquisition. Jiaojiao Shang: supervision, conceptualization, methodology, data curation, resources, funding acquisition. All authors have given approval to the final version of the manuscript.

Conflicts of interest

There are no conflicts to declare.

Abbreviations

AuNPs	Gold nanoparticles
PNIPAM	Poly(*N*-isopropyl acrylamide)
AuNPs/P(NIPAM-*co*-ABP)	Poly(*N*-isopropyl acrylamide)-*co*-4-acryloyl benzophenone embedded AuNPs
P(GMA-*co*-ABP)	Poly(glycidyl methacrylate-*co*-ABP)
PDEAEMA	Poly(diethylaminoethyl methacrylate)
MMA	Methyl methacrylate
EGCG	Epigallocatechin gallate.

Data availability

The data supporting the findings of this study are available within the article and its ESI.†

Acknowledgements

This work was supported by Institutional Research Fund from Sichuan University, China (Grant No. 2024SCUQJTX020) and the Science and Technology Project of Tibet Autonomous Region, China (Grant No. XZ202301YD0027C).

References

1 M. H. Nan, G. Go, H. W. Song, B. A. Darmawan, S. R. Zheng, S. Kim, K. T. Nguyen, K. Lee, H. Kim, J. O. Park and E. Choi, *Adv. Funct. Mater.*, 2024, **34**, 2401776.
2 Z. Chen, H. G. Wang, Y. T. Cao, Y. J. Chen, O. Akkus, H. Z. Liu and C. Y. Cao, *Matter*, 2023, **6**, 3803–3837.
3 Y. Zhao, Z. Yang and R. Zhou, *J. Bioresour. Bioprod.*, 2024, **9**, 369–378.
4 R. D. Cheng, M. W. Xu, X. H. Zhang, J. Q. Jiang, Q. Y. Zhang and Y. Zhao, *Angew. Chem., Int. Ed.*, 2023, **62**, e202302900.
5 Y. Sun, L. Chen, Z. H. Zeng, T. L. Wang, K. H. Zhang, Y. Sun, L. Yang, X. L. Feng, Q. K. Sun, C. X. Ma, S. W. Xiao, Z. Z. Liu, J. Liu and X. X. Yang, *Adv. Funct. Mater.*, 2025, **35**, 4818–4827.
6 T. Zhao, Y. Tan, Y. Li and X. Wang, *J. Colloid Interface Sci.*, 2025, **677**, 739–749.
7 L. F. Chang, D. P. Wang, Z. S. Huang, C. F. Wang, J. Torop, B. Li, Y. J. Wang, Y. Hu and A. Aabloo, *Adv. Funct. Mater.*, 2023, **33**, 2212341.
8 N. Qian, J. Hu, S. Huang, Z. Liu, M. Wang, P. Keller and H. Yang, *Angew. Chem., Int. Ed.*, 2024, **63**, e202406534.
9 Y. T. Wang, X. Zhang, S. Zhang, G. M. Yang, Y. Y. Li, Y. L. Mao, L. X. Yang, J. Y. Chen and J. Wang, *J. Mater. Chem. B*, 2024, **12**, 1495–1511.
10 W. Wang, Z. G. Wu, L. Yang, T. Y. Si and Q. He, *ACS Nano*, 2022, **16**, 9317–9328.
11 I. Apsite, S. Salehi and L. Ionov, *Chem. Rev.*, 2022, **122**, 1349–1415.
12 L. Z. Chen, F. F. Liu, T. Abdiryim and X. Liu, *Mater. Today Phys.*, 2024, **40**, 101281.
13 Y. Yu, J. J. Wang, X. Han, S. G. Yang, G. H. An and C. H. Lu, *Adv. Fiber Mater.*, 2023, **5**, 868–895.
14 W. Huo, K. Miki, H. Mu, T. Osawa, H. Yamaguma, Y. Kasahara, S. Obika, Y. Kawaguchi, H. Hirose, S. Futaki, Y. Miyazaki, W. Shinoda, S. Akai and K. Ohe, *J. Mater. Chem. B*, 2024, **12**, 4138–4147.

15 H. Zhao, Y. M. Huang, F. T. Lv, L. B. Liu, Q. Gu and S. Wang, *Adv. Funct. Mater.*, 2021, **31**, 2105544.
16 S. S. Wu, H. H. Shi, W. Lu, S. X. Wei, H. Shang, H. Liu, M. Q. Si, X. X. Le, G. Q. Yin, P. Theato and T. Chen, *Angew. Chem., Int. Ed.*, 2021, **60**, 21890–21898.
17 R. Elbaum, L. Zaltzman, I. Burgert and P. Fratzl, *Science*, 2007, **316**, 884–886.
18 W. Zhao, B. Wu, Z. Lei and P. Wu, *Angew. Chem., Int. Ed.*, 2024, **63**, e202400531.
19 Y. Hao, M. F. Qiu, K. Dai, G. Q. Zheng, C. T. Liu and C. Y. Shen, *Chem. Eng. J.*, 2025, **503**, 2310380.
20 H. Liu, R. A. Liu, K. Chen, Y. Y. Liu, Y. Zhao, X. Y. Cui and Y. Tian, *Chem. Eng. J.*, 2023, **461**, 141966.
21 M. K. Danielson and J. C. Barnes, *Matter*, 2021, **4**, 1449–1455.
22 H. Ma, Z. Cheng, X. Li, B. Li, Y. Fu and J. Jiang, *J. Bioresour. Bioprod.*, 2023, **8**, 15–32.
23 S. Eristoff, S. Y. Kim, L. Sanchez-Botero, T. Buckner, O. D. Yirmibesoglu and R. Kramer-Bottiglio, *Adv. Mater.*, 2022, **34**, 2109617.
24 D. F. Tang, C. Q. Zhang, H. N. Sun, H. Z. Dai, J. Xie, J. Z. Fu and P. Zhao, *Nano Energy*, 2021, **89**, 106424.
25 W. Yue, R. X. Xu, F. P. Sui, Y. Gao and L. W. Lin, *Adv. Funct. Mater.*, 2024, **34**, 2401159.
26 Q. Yan, R. J. Ding, H. W. Zheng, P. Y. Li, Z. L. Liu, Z. Chen, J. H. Xiong, F. H. Xue, X. Zhao, Q. Y. Peng and X. D. He, *Adv. Funct. Mater.*, 2024, **34**, 2411160.
27 Y. Gong, Y. Li, Y. Zhao, P. Li, L. Yi, P. Liu, X. Chen, J. Zhan, Y. Zheng, H. Li and F. Liu, *Chem. Eng. J.*, 2025, **515**, 163937.
28 X. N. Dong, T. Y. Guo, D. Kitagawa, S. Kobatake, P. Palffy-Muhoray and C. J. Bardeen, *ACS Appl. Mater. Interfaces*, 2022, **14**, 27149–27156.
29 Q. Yan, R. J. Ding, H. W. Zheng, P. Y. Li, Z. L. Liu, Z. Chen, J. H. Xiong, F. H. Xue, X. Zhao, Q. Y. Peng and X. D. He, *Adv. Funct. Mater.*, 2023, **33**, 2301982.
30 Y. Lee, J. Won, D.-Y. Kim and S. Park, *Small*, 2024, **21**, 2409742.
31 D. Wu, X. Li, Y. Zhang, X. Cheng, Z. Long, L. Ren, X. Xia, Q. Wang, J. Li, P. Lv, Q. Feng and Q. Wei, *Adv. Sci.*, 2024, **11**, 2400557.
32 H. Na, Y.-W. Kang, C. S. Park, S. Jung, H.-Y. Kim and J.-Y. Sun, *Science*, 2022, **376**, 301–307.
33 X. Wei, L. Chen, Y. Wang, Y. Sun, C. Ma, X. Yang, S. Jiang and G. Duan, *Chem. Eng. J.*, 2022, **433**, 134258.
34 R. Liang, H. Yu, L. Wang and D. Shen, *Adv. Funct. Mater.*, 2022, **33**, 2211914.
35 Y. Zhang, T. Zhang, Y. Gu, M. Fan, Y. Zhang, S. Wang, Y. Xia, X. Zhou and J. Xiong, *ACS Nano*, 2025, **19**, 10232–10243.